The Kinematics and Physical Properties for Some H II Regions to the North-East of NGC 4945**

Ameerah Ab. Al-Sadooni[1, a)] and Jacco Th. van Loon[2, b)]

[1]*Department of Physics, College of Science, University of Babylon, Babel, Iraq*
[2]*Lennard Jones Laboratories, Keele University, ST5 5BG, UK*

[**]*based on observations made with the Southern African Large Telescope (SALT)*

[a)] Corresponding author: sci.ameera.k@uobabylon.edu.iq
[b)] j.t.van.loon@keele.ac.uk

Abstract. We study the ionized outflows to the North-East of the edge-on spiral galaxy NGC 4945 with the combination of the Fabry-Pérot (FP) and long-slit (LS) observations at the South African Large Telescope (SALT). The FP observation was used to analyse Hα emission, introduce first map of ionized outflows (Hα), continuum, kinematic map (the velocity and velocity dispersion) from some H II regions and SNRs to quantify their impact on the surroundings. Different filaments of ionized gas were traced as well as, bubble shape structure could extended from giant H II region (A3), which shows structure as a feedback onto surroundings. The LS observation introduced the physical properties in these areas with more details by tracing Hα and Hβ as recombination lines and ([N II]λλ6549,6583, [S II]λλ6717,6731 as forbidden lines. The diagnostic diagram based on two ratios (Hα/[N II] and Hα/[S II]) was used to determine the type of these regions which eject ionized outflows. The determined electron densities in the selected regions show a range of values between 2 to 860 cm^{-3}, the highest value appears in region that shows properties of SNR. The oxygen and nitrogen abundances were calculated by using N2 and N2S2 indices for H II regions and SNRs. The oxygen abundances are stable within (2 – 6) kpc of the galactocentric distance, while the abundance of nitrogen rises with increasing the galactocentric distance. The correlation between oxygen and nitrogen abundances presents a mild negative with high metallicity

Keywords: Galaxy: formation, evolution, abundances, H II, disc.

INTRODUCTION

The internal processes in the rotating disk of galaxies, such as star formation, supernova explosion (SNe) and active galactic nuclei (AGN) introduce important mechanism by which the energy and matter are recycled in galaxies. Hence, it may have extraplanar material in form of galactic fountain [1], chimney, and galactic winds [2]. Although the star formation and supernovae occur at small scale (1 pc) [3] but their feedback on the surrounding interstellar medium (IMS) extends to galactic scales [4]. The deposit material and energy can re-shape the distribution of gas resulting in filaments or bubble structures [5, 6].

The information of the chemical composition of spiral galaxies, in particular from H II regions, is a key for understanding their evolution. The ionized outflows from active regions can afford with the initial abundances from which stars are created. Abundance gradients have been traced in many spiral galaxies and display that the abundances of metals decline outward from the galactic center [7, 8]. Radial abundance gradients of metals relative to hydrogen in spiral galaxies have been introduced by various models of galactic chemical evolution [9, 10]. The oxygen is the third highest abundant element in the Universe. It is usually treated as an alternate of the metallicity in photoionized nebulae. The oxygen is about completely produced by massive stars (M > 8Mo) and in short time scale, the oxygen ejected to the interstellar medium by type II supernovae explosions. While, the carbon and nitrogen were originated in more complicated processes, which follow different procedures in different stellar mass ranges [11, 12]. There are two different procedures to determined abundances of elemental gas: the direct method of

3rd International Scientific Conference of Alkafeel University (ISCKU 2021)
AIP Conf. Proc. 2386, 080049-1–080049-12; https://doi.org/10.1063/5.0067075
Published by AIP Publishing. 978-0-7354-4150-7/$30.00

electron temperatures [13], where the faint auroral lines ([O III]λ4363 and [N II]λ5755) can be observed, otherwise, the strong line methods can be used to derive the elemental gas abundances. Different strong line diagnostics can be used to determine the oxygen and nitrogen abundance by applying empirical calibrations [14, 15, 16, 17, 18]

NGC 4945 is nearby spiral galaxy with morphological type SA(s)d [19], located at a distance of 3.58 Mpc [20], and the inclination of NGC 4945 is ≈ 78˚ [21]. This galaxy could be having similar size, mass, and morphological type to the Milky Way. NGC 4945 shows ejected cone from the nucleus which is a subject for various studies using Fabry-Perot, long-slit, and imaging such as [22, 23, 24] to study the morphological and kinematical properties of the ionized outflows. But the rest of the galaxy has not yet observed to study the kinematics and distribution of the ionized outflows from giant H II regions. The main purpose of this study is to introduce first morphological and kinematic maps for ionized gas within giant H II regions to the North East of the galaxy by using Fabry-Pérot spectral imaging with the medium-resolution. The Fabry-Pérot with SALT can be unique tool to map strongest optical line Hα. In order to get more information about the physical properties and chemical compositions of the regions with high ionized emission, the long-slit spectroscopy mode was used to re-observe these regions. The paper is organized as follows. In section 2, the observations and general description of the data reduction were introduced. Analysis and discussion were presented. Finally, in section 3, we introduced the main conclusions.

OBSERVATION AND DATA PROCESSING

Fabry-Pérot Imaging Spectroscopy The target region of NGC 4945 was observed in Fabry-Pérot mode in one field (8̀) of view with centre (RA: $13^h\ 5^m\ 48.7^s$, Dec: - 49˚24` 43.6¨). The observations were done on 15th August 2015 to trace Hα emission with medium resolution (MR; R ≈ 1400). The imaging spectroscopic mode was adopted to cover a spectral region of (6570 - 6584) Å with 8 step (2 Å separation, integration time = 85.2 s) to cover the Hα line and continuum, after take into consideration the systemic velocity of NGC 4549 (563 km s^{-1}) [25]. The reduction of FP was done by following different steps: bias subtraction, dark frame subtraction, mask, ghost removing, flat fielding, flux calibration and scaling, wavelength calibration, sky-lines calibration, and finally fitting the line profile with a Voigt function to determine the maximum intensity (I_o), wavelength (λ_o) at I_o and its uncertainty $\Delta\lambda_o$ (velocity dispersion), more information about previous reduction can be found in Al-Sadooni [24], Mitchell et al. [26]Long-Slit Spectroscopy.

The spectra were achieved at SALT 10 m telescope on 2017 January 19th. The width of the slit was 1¨. The center of the slit is at (RA: $13^h\ 5^m\ 34^s$, Dec: - 49˚25` 59¨).

The slit was oriented with position angle that equals 49˚. The two VPH gratins (PG3000 and PG2300) were used with the E2V CCD 44-82 chips, producing a reciprocal dispersion of 0.268 Å pixel $^{-1}$, a resolution of 0.76 Å and 1 Å respectively. The two gratings allowed us to trace red and blue lines that are in two spectral range (4335 – 5016 and 5904 – 6755) Å and the exposure time for each range is 300 second. The comparison arc lamp of Ne and CuAr were used in the wavelength calibration. The summary of observations are listed in Table 1. The steps of the long-slit reduction including bias and dark subtraction and flt-field-correction, remove cosmic ray impacts from frames, wavelength calibration and sky-subtraction, were carried out using the PySALT SALTSPEC package [27], PyRAF and IRAF (The Image Reduction and Analysis Facility). The extracted spectra from the 2D frames were determined by using IRAF, and the fitting processes and plotting were done by using Python.

TABLE 1. Summary of FP and LS observations.

Telescope	SALT	
Instrument	RSS	
Detector	E2V CCD 44-82 chips	
Pixel scale[¨pixel^{-1}]	0.5068	
Reciprocal dispersion [(Å pixel^{-1}]	0.268	
Mode	Long-slit	Fabry-Pérot
Date of observation	19th January 2017	15th August 2015
Grating [s]	PG3000 & PG2300	…
Slit width	1¨	…
Exposure time [second]	300	85.2
Spectral resolution [Å]	0.76 & 1	…
Resolving power	…	≈ 1400
Filter	…	PI06530
Free spectral range [Å]	…	75
Steps	…	8
Slit center (PA = 49 ˚)	RA: 13^{h} 5^{m} 34^{s}	…
	Dec: - 49 ˚25 `59 ¨	…
Field center (PA = 43 ˚)	…	RA: 13^{h} 5^{m} 48.7^{s},
	…	Dec: - 49˚24` 43.6¨

RESULT AND ANALYSIS

The Distribution of Hα Emission in the Observed FP Field In order to trace the feedback of ionized outflows on the surrounding ISM in forms of interaction between them, deep observation of FP was analysed. This process can help to identify H II regions and extract kinematics. The observed total intensity of the emission (continuum and Hα) of FP field is shown in Fig. 1. The total intensity was determined by adding all intensities along the wavelength axis of the FP cube. The dark edge in Fig. 1 represent CCD gaps, and the dark area in the bottom right represents a guiding probe. Different objects appear in the field with various size and morphological structures across a region of ≈ 8` diameter. As well as, foreground stars spread as bright dots in different positions in the field. The red cross refers to the center of the galaxy. The cone is obvious to the North-East of the center.

After examining the Hα profile across the FP field, there is no sign of split. Therefore, the fitting parameters of Hα emission were determined from a single Gaussian fit for the observed field and shown in Fig. 2: (a) shows the continuum. (b) maximum intensity of Hα, (c) velocity and (d) velocity dispersion. From the adopted wavelength range, the velocity are between – 200 to 200 km s^{-1} which are expected of the outflowing gas from H II regions. Hence, the high velocities of outflows from the centre of NGC 4945 are not detectable from these observations. High intensity of the ionized phase concentrates in specific positions representing H II regions along the spiral arm (North- East) of the galaxy (see panel (b) in Fig. 2). NGC 4945 shows two spirals, one to the North- East and second one to the South West. Along the first arm (observed field) 8` prominent objects appears with a range of radii from 400 pc to 1 kpc (A1 – A8) which are labeled in panel (b) Fig. 2. Many smaller areas with ≈ 150 pc or less, as well as clear filaments connect between these areas. The A3 object shows interesting morphological structures as it is clear in the Hα emission (see panel (b)). The A3 object spans about 500 pc and connects to clear extended filaments to form bubble shape with ≈ 1 kpc in diameter. The highest Hα emission ejects from the object A6, which extends to ≈ 1 kpc. Prominent two filaments connect between A6 and A7 like bridge to the South West of the A6. Many smaller regions and filaments to the North of the A6 and East of A7 may be related to A6 and A7 or could be projection effect. The A5 object could be filaments or faint H II region, as this part of the galaxy is partially obscure. The cone structure from the centre of the galaxy did not included in this study because the kinematic of the cone structure is

out of the observed range of the wavelength, however, it was studied in details by [2]. In order to determine the physical properties of some of these large objects in details, we re-observed these regions with long slit mode (the black line in panel (b)

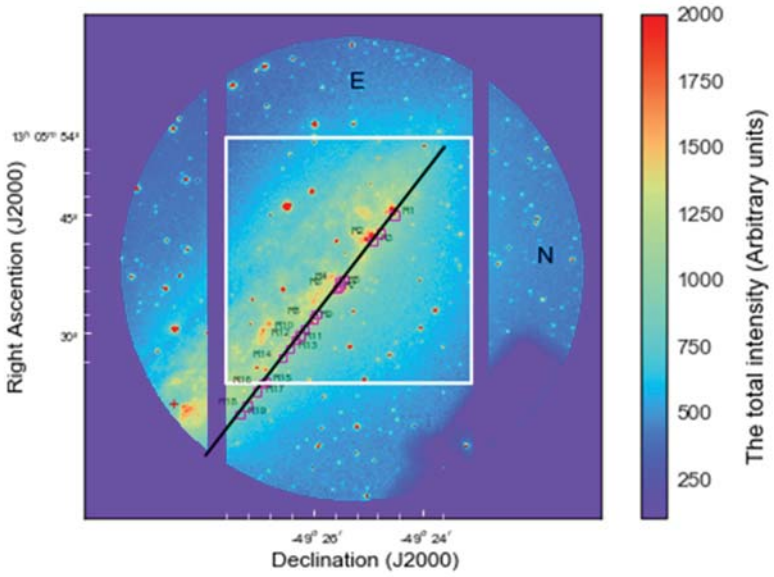

FIGURE 1. The total intensity map of the data cube of Hα. The centre of the observed field is RA: (13^h 5^m 48.7^s, Dec: - 49˚ 24` 43.6˜)

The centre of NGC 4945 is marked with the red cross symbol. The North and East of the galaxy are marked to the right and top of the Fig.2. The while square zoomed into the four panels in Fig. 2. The Kinematics of Hα Emission in the FP Field Fig. 2 panel (c) presents the kinematic map of the Hα emission in the observed field. In general the traced velocities range between -100 and 200 km s^{-1}. The target A1 shows velocities about 200 km s^{-1} in the central area and reduce radially.

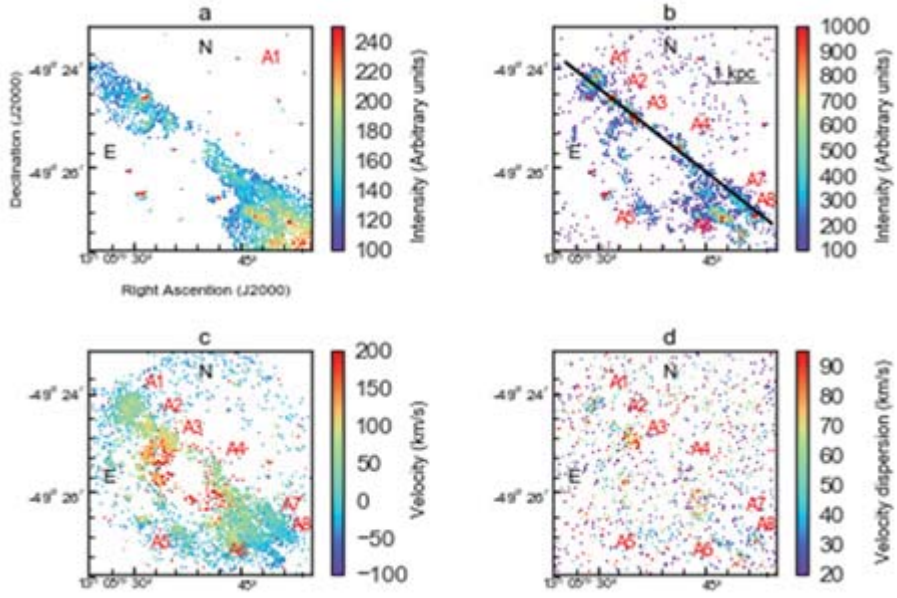

FIGURE 2. The fitted cube of Hα of the observe field (13^h 5^m 48.7^s, Dec: - 49˚24` 43.6˜). (a) is the continuum, (b) represents the maximum intensity of the profile. (c) and (d) show the velocity and velocity dispersion.

While A2 and A3 show velocities ≈ 200 km s^{-1}, likewise the filaments that form the bubble shape display velocities ≈ 200 km s^{-1}. The velocities of the outflows in objects A7 and A8 are 10 to 60 km s^{-1}. The outflowing gas in A6 show a wide range of velocities between a few km s^{-1} to 200 km s^{-1}. The velocity dispersion map (Fig. 2 panel (d)) shows values between 20 to 90 km s-1 in selected objects. The A1 displays high velocity dispersion (≈ 90 km s^{-1} and reduces in the outer regions (50 km s^{-1}). While A3 shows high values of velocity dispersion in the outer boundaries and increase to reach ≈ 90 km s^{-1}

Spectral Analysis of the LS

The prominent targets (A1, A2, A3, A4, A7, A6) in FP field that located along the spiral arm were re-observed by LS mode (see panel (b) Fig. 2) in order to determine the physical conditions in these large targets. Fig. 3 shows 20 targets that have clear Hα emission. The emission spectra of each target were plotted and the prominent emission lines were fitted with a single Gaussian components to extract their parameters by using MPFIT package. The Doppler effect along the line of sight was used to determine the kinematics (the radial velocity and velocity dispersion) of each region from Hα, Hβ, [N II]λλ6549,6583 and [S II]λλ6717,6731, and summarized in Table 2. The R7 and R8 display the maximum velocity dispersion from all the emission lines, which is in a range of (80-110) km s^{-1}. While the minimum value (≈ 50 km s^{-1}) appears in R11 and R19. The rotation curve to the North- East side from the centre of NGC 4945 was determined, from the radial velocities of Hα emission to approximately 6 kpc (Fig. 4) by assuming a flat plane, zero thickness and circular orbit.

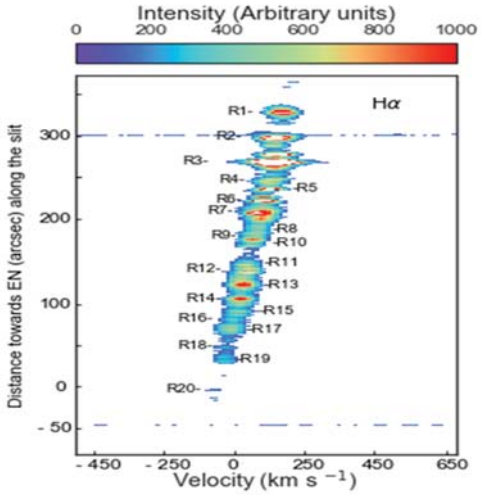

FIGURE 3. Spatial and kinematic map of the Hα line along the slit. The spectral dispersion axis was converted into heliocentric Doppler velocity for Hα line. Zero arcsec marks the place on the slit closest to the galaxy centre. The selected regions are labeled.

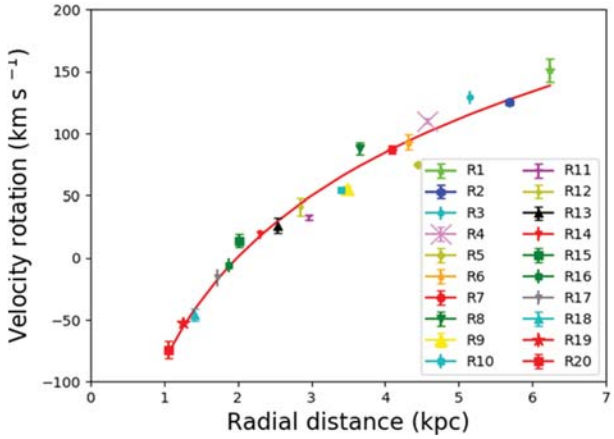

FIGURE 4. The rotation curve of NGC 4945 determined from Hα emission to the North-East side of the centre.

TABLE 2. Centroid velocity and full-width at half maximum of 20 emission-line objects in NGC 4945.

Object	Hα		[N II]		[S II]		Hβ	
	Velocity [km s^{-1}]	FWHM [km s^{-1}]	Velocity [km s^{-1}]	FWHM [km s^{-1}]	Velocity [km s^{-1}]	FWHM [km s^{-1}]	Velocity [km s^{-1}]	FWHM [km s^{-1}]
R1	140 ± 9	69 ± 9	140 ± 9	74 ± 1	125 ± 7	72 ± 8	159 ± 6	92 ± 9
R2	116 ± 2	77 ± 2	115 ± 7	71 ± 1	100 ± 5	82 ± 5	133 ± 4	84 ± 4
R3	119 ± 5	73 ± 4	119 ± 4	71 ± 3	103 ± 5	69 ± 7	127 ± 3	80 ± 6
R4	101 ± 2	65 ± 4	101 ± 5	62 ± 9	78 ± 9	64 ± 3	104 ± 3	69 ± 4
R5	68 ± 1	68 ± 2	80 ± 3	66 ± 4	67 ± 8	60 ± 5	99 ± 6	57 ± 4
R6	85 ± 6	65 ± 8	85 ± 3	68 ± 2	77 ± 9	73 ± 2	99 ± 5	65 ± 6
R7	80 ± 3	85 ± 7	81 ± 5	83 ± 4	60 ± 9	100 ± 7	87 ± 8	94 ± 4
R8	80 ± 5	85 ± 4	81 ± 9	83 ± 8	60 ± 7	98 ± 5	71 ± 9	108 ± 7
R9	50 ± 3	62 ± 5	52 ± 9	56 ± 2	37 ± 8	89 ± 7	63 ± 2	77 ± 7
R10	49 ± 3	72 ± 9	48 ± 5	73 ± 5	29 ± 9	69 ± 7	…	…
R11	29 ± 2	60 ± 9	43 ± 3	61 ± 4	15 ± 9	49 ± 2	55 ± 2	83 ± 7
R12	36 ± 7	67 ± 5	39 ± 2	65 ± 5	23 ± 8	62 ± 4	32 ± 5	100 ± 8
R13	22 ± 6	70 ± 9	24 ± 3	70 ± 5	7 ± 8	78 ± 8	29 ± 3	60 ± 5
R14	16 ± 4	62 ± 4	16 ± 5	57 ± 9	3 ± 9	53 ± 9	23 ± 6	120 ± 7
R15	11 ± 5	57 ± 6	9 ± 2	65 ± 7	-12 ± 9	72 ± 9	37 ± 2	148 ± 7
R16	- 4 ± 6	68 ± 5	-12 ± 4	94 ± 3	-25 ± 5	81 ± 9	-10 ± 10	34 ± 7
R17	-12 ± 7	71 ± 4	-13 ± 2	92 ± 4	-26 ± 7	57 ± 9	-8 ± 5	55 ± 6
R18	-29 ± 5	73 ± 3	-26 ± 2	88 ± 4	-55 ± 2	5 8± 6	-11 ± 2	74 ± 8
R19	-26 ± 4	63 ± 8	-33 ± 4	59 ± 2	-46 ± 4	48 ± 9	-11 ± 4	73 ± 8
R20	-57 ± 7	55 ± 5	-74 ± 5	63 ± 2	-71 ± 9	58 ± 8	…	…

Physical Conditions of Selected Targets

The ionized nebulae show a week continuum and bright emission lines in their spectra by three main procedures: recombination, collisional excitation and photo-excitation. These lines provide an effective method to drive the physical conditions of the gas, electron density and electron temperatures. The LS spectra display the most conspicuous emission lines in ionized nebulae, such as recombination and forbidden lines (Hα and Hβ, [N II] λλ6549,6583 and [S II]λλ6717,6731). The appearance of recombination and de-excitation lines represent the important sources of cooling in the nebula, where the captured photon loses its kinetic energy in order to produce these emission lines. The important ratios were listed in Table 3.

The identification of these selected regions was made using forbidden line ratios Hα/[N II] and Hα/[S II] to place our 20 targets within diagnostic diagram which categorizes between H II regions, supernova remnants and planetary nebulae [28, 29]. The current mechanism that controls the excitation of the gas can be determined by the diagnostic diagram. The 20 regions fall in the classic diagnostic of log(Hα/[S II]) and log(Hα/[N II]) ranges of (0.18-0.63) and (0.2) respectively (see Fig. 5). Three target fall well within the defined zone for SNR, seven targets locate H II regions. Four targets fall in the boundary of H II zone and the error bar of these regions extends highly in the photonized gas zone, therefore we will deal with these four targets as H II regions. Six targets locate the zone between the three distinguished zones.

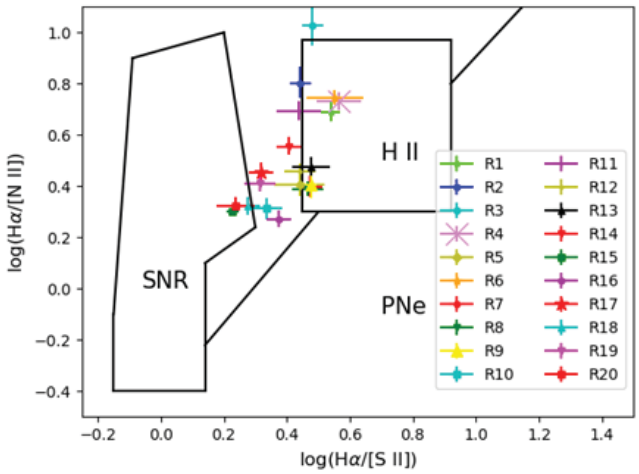

FIGURE 5. The 20 emission-line objects in NGC 4945 are shown on the diagnostic diagram depending on the ratios of Balmer recombination line (Hα) and collisionally excited lines ([S II] and [N II]. The boundaries are adapted from Camps-Fariña *etal*. (2017) [29].

TABLE 3. Emission line ratios of 20 emission- line objects in NGC 4945.

Object	[S II]/Hα	[N II]/Hα	Hα/Hβ	log([NII]/Hα	log([SII]/Hα)
R1	0.20 ± 0.02	0. 29± 0.01	22.80 ± 0.00	-0.54	-0.69
R2	0. 16 ± 0.05	0.36 ± 0.07	16.80 ± 0.00	-0.44	-0.8
R3	0.09 ± 0.03	0.33 ± 0.09	24.40 ± 0.00	-0.48	-1.03
R4	0.18 ± 0.04	0.27 ± 0.01	33.50 ± 0.09	-0.56	-0.73
R5	0. 39 ± 0.01	0.38 ± 0.01	13.79 ± 0.20	-0.41	-0.40
R6	0. 18 ± 0.03	0.28 ± 0.01	46.34 ± 0.00	-0.55	-0.75
R7	0. 40 ± 0.01	0.33 ± 0.02	14.30 ± 0.85	-0.47	-0.40
R8	0. 40 ± 0.01	0.34 ± 0.01	21.97 ± 0.06	-0.46	-0.39
R9	0.39 ± 0.04	0.33 ± 0.05	22.50 ± 0.00	-0.47	-0.40
R10	0.48 ± 0.01	0.34 ± 0.01	…	-0.33	-0.31
R11	0.20 ± 0.04	0.33 ± 0.01	26.01 ± 0.20	-0.44	-0.69
R12	0.34 ± 0.01	0.46 ± 0.01	14.34 ± 0.70	-0.41	-0.45
R13	0.33 ± 0.03	0.36 ± 0.01	21.46 ± 0.06	-0.48	-0.47
R14	0.27 ± 0.03	0.38 ± 0.06	15.40 ± 0.00	-0.40	-0.55
R15	0.50 ± 0.01	0.33 ± 0.01	6.50 ± 0.00	-0.23	-0.30
R16	0.53 ± 0.01	0.39 ± 0.02	18.55 ± 0.00	-0.36	-0.27
R17	0.35 ± 0.01	0.59 ± 0.02	17.32 ± 0.09	-0.32	-0.45
R18	0.47 ± 0.01	0.43 ± 0.02	10.80 ± 0.09	-0.27	-0.32
R19	0.38 ± 0.01	0. 48 ± 0.01	8.29 ± 0.01	-0.31	-0.41
R20	0.47 ± 0.00	0.57 ± 0.01	…	-0.29	-0.32

The Determination of Electron Density

We could in principle also use the [S II]λ6717/[S II]λ6731 ratio as an indicator of the electron density (N_e). 15 regions show values that are within the range in which the ratio is sufficiently sensitive to the density [30]. In this work, we calculate the N_e (adopting case B (T = 10,000 k)) [30] by using Eq. 1 [31]:

$$\frac{I([S\ II]\lambda 6717)}{I([S\ II]\lambda 6731)} = 1.49\ \frac{1+3.77\,\chi}{1+12.8\,\chi}. \qquad (1)$$

Where the parameter χ represents $\mathbf{10^{-4}\ Ne\ T_e^{-1/2}}$. The χ and T_e refer to the density parameter and temperature of the electron in units of 10^4 K, respectively. The highest value of the N_e is ≈ 860 cm^{-3} which appears in SNR (R18), while the minimum value (2 cm^{-3}) appears in H II regions (R8). The value of N_e in the selected regions are shown in Table 4.

TABLE 4. Classifications and electron density determinations.

Region	Type	N_e [cm^{-3}]	Region	Type	N_e [cm^{-3}]
R1	H II	440	R11	H II	…
R2	H II	50	R12	H II	…
R3	H II	18	R13	H II	348
R4	H II	265	R14	…	40
R5	H II	139	R15	SNR	346
R6	H II	355	R16	…	…
R7	H II	10	R17	…	…
R8	H II	2	R18	SNR	862
R9	H II	105	R19	…	…
R10	…	…	R20	SNR	…

DISCUSSION

The Trends of N2 and N2S2 Indices. The relationship between the abundance of nitrogen relative to oxygen and the oxygen abundance *(12 + log(O/H)*) is well studied in disc galaxies [32, 33, 34, 35]. Fig. 6 displays *log(N/O)* versus *12 + log(O/H)* for the H II regions and SNRs in the sample of study in NGC 4945 (the determined values are listed in Table 5). The three SNRs (red circles) display nitrogen abundance that is about the solar value. While H II regions show values high and less than the solar value in a range of (-0.968 - 0.407). Overall, the oxygen aboundances calculated in this paper are all relatively high (*12 + log(O/H)*; average *12 + log(O/H)* = 8.541) as we expect that the sample locates in high-metallicity regime [36, 37, 38]. The black dashed line represents the best fit to the H II regions in the current sample which calculated from N2 index (*log([N II]λ6583/Hα*). As we mentioned before the traced spectra did not show auroral lines [O III]λ4363 and [N II]λ5755. The trend of N/O with O/H is constant at low metallicities and rise with important role to diffuse the correlation between N/O and O/H. The much of the scatter between the *log(N/O)* versus *12 + log(O/H)* relation could be illustrated by the time delay between creating oxygen and secondary nitrogen [39]. The studied sample (H II and SNRs) displays approximately a mind negative slope (Pearson correlation coefficient r = - 0.126) contrast to what appears to the South-East of NGC 4945 for the same range of metallicity and radial distance, where the Pearson correlation coefficient is 0.75 40. An important aspect we have to remark in Fig. 4 and Fig. 6 in [40], is the lack of any clear trend in the distribution of N/O ratios with respect to O/H in the range of 8.45 - 8.70 in *12+log(O/H)*, as it usually traced in other Galaxies (e.g. [7]

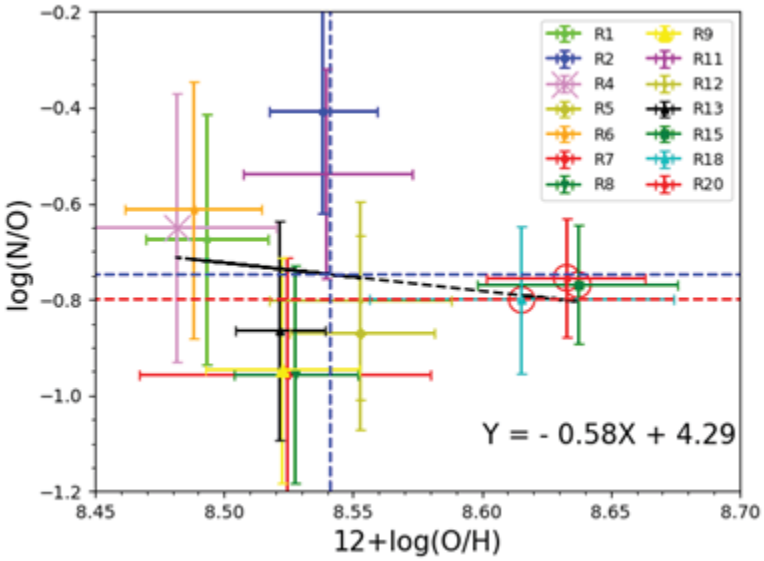

FIGURE 6. Trends of Nitrogen-to-oxygen with oxygen abundance for 11 H II and 3 SNRs emission-line objects in NGC 4945.

The best-fit linear regression (black dashed line) was determined from 11 H II. The blue dashed lines show the medians of *log(N/O) and 12+ log(O/ H)*. The red dashed line represents the solar value. The SNRs are marked by red circles.

Radial Abundance Gradients

Fig. s 7 and 8 show the trend of the O/H and N/O ratios with radial distance. The latter is determined by taking into account the inclination of the disk and the slit offset from the center of NGC 4945. In Fig. s 7 and 8, the targets or their error bars that locate within the boundaries of H II or SNRs are shown. The SNRs are marked with red circle and the linear regression fits of oxygen abundance and nitrogen abundance as a function of the radial distance are shown with green (H II) and black (H II and SNRs) lines. All parameters of the linear regressions fits summarized in Table 6.

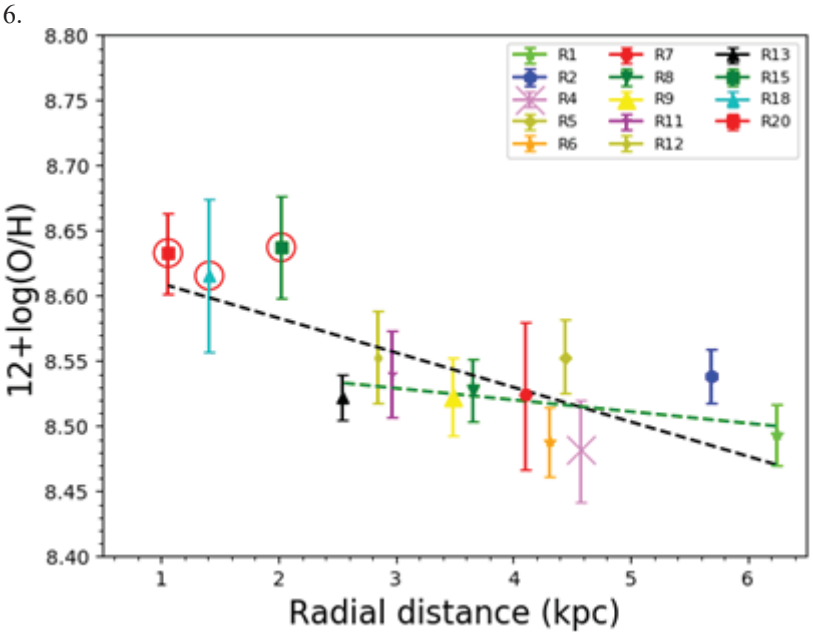

FIGURE 7. Radial variation of the oxygen abundance for 11 classical H II emission-line objects in NGC 4945.

Red circles represent SNRs.The black dashed line represents the best-fit linear regression for H II and other objects, while the green lines is fit for only classical H II regions from the *N2* index.

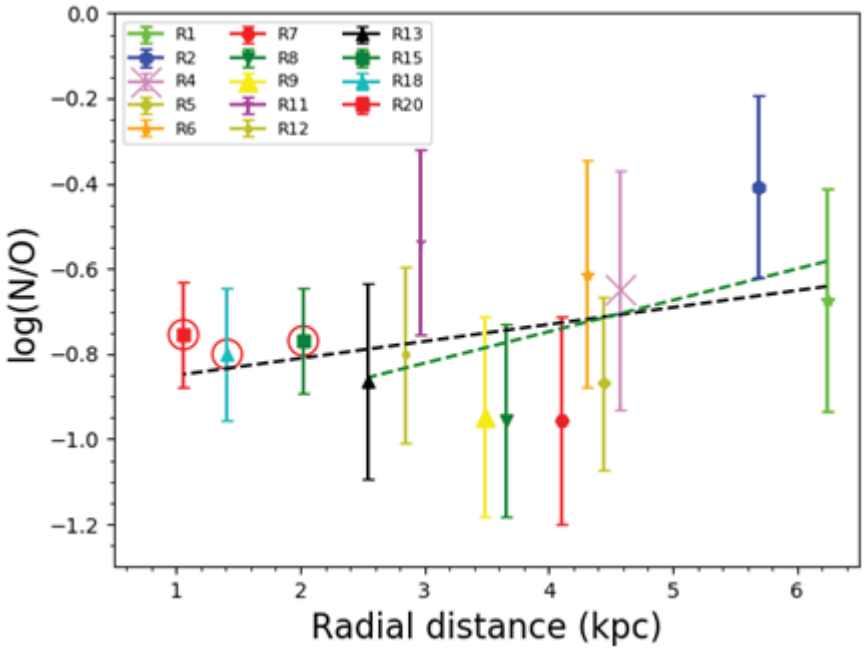

FIGURE 8. Radial variation of the nitrogen-to-oxygen ratio for 14 (H II regions and SNRs) emission-line objects in NGC 4945.

The black dashed line is the best-fit linear regression to all 14 objects: the green and red line is the fit for just the classical H II regions.

TABLE 5. The trend of N with O/H.

Region	R [kpc]	N2→ 12+log(O/H)		N2S2→ 12+log(O/H)	
R1	6.24	-0.540	8.493	-0.147	-0.673
R2	5.68	-0.443	8.538	-0.359	-0.407
R3	5.15	-0.481	8.520	-0.545	-0.172
R4	4.57	-0.566	8.481	-0.166	-0.650
R5	4.43	-0.411	8.552	-0.007	-0.870
R6	4.31	-0.551	8.488	-0.196	-0.613
R7	4.09	-0.473	8.524	-0.076	-0.956
R8	3.65	-0.466	8.527	-0.076	-0.956
R9	3.48	-0.476	8.522	-0.069	-0.947
R10	3.39	-0.334	8.588	-0.021	-0.886
R11	2.96	-0.439	8.539	-0.256	-0.537
R12	2.84	-0.411	8.552	-0.046	-0.801
R13	2.54	-0.478	8.521	-0.004	-0.864
R14	2.29	-0.406	8.555	-0.149	-0.671
R15	2.02	-0.229	8.637	-0.072	-0.769
R16	1.87	-0.357	8.577	-0.086	-0.968
R17	1.72	-0.318	8.595	-0.136	-0.687
R18	1.41	-0.276	8.615	-0.047	-0.800
R19	1.26	-0.316	8.597	-0.096	-0.738
R20	1.05	-0.238	8.632	-0.083	-0.754

TABLE 6. parameters of the linear fits of the radial variation of oxygen and nitrogen abundance for emission-line regions in NGC 4945, and the Pearson correlation coefficient *r*.

Abundance	Type	Slope [dex kpc^{-1}]	Intercept	No.	Index	*r*
12+log(O/H)	H II+SNRs	-0.026	8.635	14	*N2*	-0.763
12+log(O/H)	H II	-0.010	8.556	11	*N2*	-0.394
log(N/O)	H II + SNRs	-0.039	-0.889	14	*N2S2*	0.358
log(N/O)	H II	-0.073	1.043	11	*N2S2*	0.443

CONCLUSIONS

We present the first kinematic map for the North-East side of the edge-on NGC 4945 based on FP observations of the Hα emission line. The morphology of the ionized outflows from star-formation regions were mapped to show the impacts of the ejected material on the surroundings. Different morphological structures appears in form of filaments and bubble shape. These targets were re-observed with long-slit spectroscopy in order to trace more emission lines, that are important to estimate the physical properties in these targets by studying the shape of the emission lines. The present-day chemical abundances were determined across these areas based on N2 and N2S2 indices. The radial abundance gradients were examined in the disc of NGC 4945.

ACKNOWLEDGEMENTS

We thank the staff at SALT for their support in carrying out the observation for this study, and Keele University for their generous time allocation. We are indebted to the Ministry of Higher Education and Scientific Research. Iraq for providing financial support. Finally, we are very appreciate to university of Babylon for their support during the research. .

REFERENCES

1. F. Fraternali and J. J. Binney, Monthly Notices of the Royal Astronomical Society. 366, (2006) 449-466.
2. D. Breitschwerdt, J. F. McKenzie, and H. J. Voelk, Astronomy and Astrophysics. 245, (1991) 79-98.
3. A. Dekel and J. Silk, Astrophys. J. 303, (1986) 39.
4. D. Ceverino and A. Klypin, The Astrophysical Journal. 695, (2009) 292–309.
5. R. A. Chevalier and A. W. Clegg, Nature (London). 317, (1985) 44.
6. R. Weaver, R. McCray, J. Castor, P. Shapiro, and R. Moore, Astrophys.J. 218, (1977) 377-395.
7. C. Esteban, F. Bresolin, J. García-Rojas, and L. T. San Cipriano, Monthly Notices of the Royal Astronomical Society. 491. 2. (2019) 2137-2155.
8. K. Z. Arellano-Córdova, C. Esteban, J. García-Rojas, and J. E. Méndez-Delgado, Monthly Notices of the Royal Astronomical Society. 496, (2020) 1051–1076.
9. M. Palla ,F. Matteucci, E. Spitoni, F. Vincenzo, and V. Grisoni, Monthly Notices of the Royal Astronomical Society 498, 2, (2020) 1710-1725.
10. V. Grisoni, E. Spitoni, and F. Matteucci, Monthly Notices of the Royal Astronomical Society 481, (2018) 2570-2580.
11. C. Chiappini, D. Romano, and F. Matteucci, Monthly Notices of the Royal Astronomical Society 339, (2003) 63-81.
12. L. Carigi, M. Peimbert, C. Esteban, and J. Garcia-Rojas, The Astrophysical Journal 623, (2005) 213.
13. L. J. Kewley and S. L. Ellison, Astrophys. J. 681, (2008) 1183-1204.
14. R. A. Marino, F. F. Rosales-Ortega, S. F. Sánchez, A. Gil de Paz,J . Vílchez, D. Miralles-Caballero, C. Kehrig, E. Pérez-Montero, V. Stan-ishev, J. Iglesias-Páramo, A. I. Díaz, A. Castillo-Morales, R. Kennicutt,A. R. López-Sánchez, L. Galbany, R. García-Benito, D. Mast, J. Mendez-Abreu, A. Monreal-Ibero, B. Husemann, C. J. Walcher, B. García-Lorenzo,J. Masegosa, A. Del Olmo Orozco, A. M. Mourão, B. Ziegler, M. Mollá,P. Papaderos, P. Sánchez-Blázquez, R. M. González Delgado, J. Falcón-Barroso, M. M. Roth, G. van de Ven, and Califa Team, Astronomy and Astrophysics 559, A114 (2013).

15. T. Storchi-Bergmann, D. Calzetti, and A. L. Kinney, Astrophys. J. 429, 572-581 (1994).
16. G. Denicoló, R. Terlevich, and E. Terlevich, Monthly Notices of the Royal Astronomical Society 330, 69-74 (2002).
17. E. Pérez-Montero and T. Contini, Monthly Notices of the Royal Astronomical Society. 398, (2009) 949-960.
18. L. Stanghellini, L. Magrini, and V. Casasola, The Astrophysical Journal. 812, (2015) 39 .
19. H. G. Corwin, Jr. , A. de Vaucouleurs, and G. de Vaucouleurs, Astronomical Journal 83, (1978) 1566-1580.
20. A. Monachesi, E. F. Bell, D. J. Radburn-Smith, J. Bailin, R. S. de Jong,B. Holwerda, D. Streich, and G. Silverstein, Monthly Notices of the Royal Astronomical Society 457, (2016) 1419-1446.
21. M. Dahlem, G. Golla, J. B. Whiteoak, R. Wielebinski, S. Huettemeister,and C. Henkel, Astronomy and Astrophysics 270, (1993) 29-42.
22. S. Lípari, Z. Tsvetanov, and F. Macchetto, Astrophysical Journal, Supplement 111, (1997) 369-375.
23. T. M. Heckman, L. Armus, and G. K. Miley, Astrophysical Journal, Supplement. 74, (1990) 833-868.
24. A. Ab. Al-Sadooni, "The impact of ionized outflows on the surrounding inter-stellar medium in disc galaxies", PhD thesis, Keele university, 2018.
25. B. S. Koribalski, L. Staveley-Smith, V. A. Kilborn, S. D. Ryder, R. C.Kraan-Korteweg, E. V. Ryan-Weber, R. D. Ekers, H. Jerjen, P. A. Henning, M. E. Putman, M. A. Zwaan, W. J. G. de Blok, M. R. Calabretta, M. J. Dis-ney, R. F. Minchin, R. Bhathal, P. J. Boyce, M. J. Drinkwater, K. C. Free-man, B. K. Gibson, A. J. Green, R. F. Haynes, S. Juraszek, M. J. Kesteven, P. M. Knezek, S. Mader, M. Marquarding, M. Meyer, J. R. Mould, T. Oosterloo, J. OBrien, R. M. Price, E. M. Sadler, A. Schröder, I. M. Stewart,F. Stootman, M. Waugh, B. E. Warren, R. L. Webster, and A. E. Wright,The Astronomical Journal128, (2004) 16-46.
26. C. J. Mitchell, J. A. Sellwood, T. B. Williams, K. Spekkens, R. Kuzio deNaray, and A. Bixel, Astronomical Journal 155, (2018) 123.
27. S. M. Crawford, M. Still, P. Schellart, L. Balona, D. A. H. Buckley, G. Dug-more, A. A. S. Gulbis, A. Kniazev, M. Kotze, N. Loaring, K. H. Nordsieck,T. E. Pickering, S. Potter, E. Romero Colmenero, P. Vaisanen, T. Williams, and E. Zietsman, PySALT: the SALT science pipeline, in Observatory Operations: Strategies, Processes, and Systems III, Vol. 7737, 773725 (2010).
28. F. Sabbadin, S. Minello, and A. Bianchini, Astronomy and Astrophysics. 60, (1977) 147-149.
29. A. Camps-Fariña, J. E. Beckman, J. Font, A. Borlaff, J. Zaragoza-Cardiel,and P. Amram, Monthly Notices of the Royal Astronomical Society. 461, (2016) 87-91.
30. D. E. Osterbrock, Astrophysics of gaseous nebulae and active galactic nuclei 1989.
31. M. L. McCall, Monthly Notices of the Royal Astronomical Society 208, (1984) 253-259.
32. M. L. McCall, P. M. Rybski, and G. A. Shields, Monthly Notices of the Royal Astronomical Society. 57, (1985) 1-62.
33. R. B. C. Henry, K. B. Kwitter, and J. A. Bates, Astrophys. J. 531, 928-941 (2000).
34. F. Bresolin, W. Gieren, R. P. Kudritzki, G. Pietrzy´nski, M. A. Urbaneja, and G. Carraro, Astrophys. J.700, (2009) 309-330.
35. Vincenzo, Fiorenzo and Kobayashi, Chiaki, A&A. 610, (2018) .
36. M. B. Vila-Costas and M. G. Edmunds, The Royal Astronomical Society. 265, (1993) 199-212.
37. Y. I. Izotov and T. X. Thuan, Astrophys. J. 511, (1999) 639-659.
38. D. A. Berg, E. D. Skillman, A. R. Marble, L. van Zee, C. W. Engelbracht, J. C. Lee, R. C. Kennicutt, D. Calzetti, D. A. Dale, and B. D. Johnson, The Astrophysical Journal. 754, (2012) 98.
39. D. R. Garnett, Astrophys. J. 363, (1990) 142.
40. H. A. Hamza, A. Ab. Al-Sadooni, and J. Th. V. Loon, NeroQuantology 18, 12, (2020) 6-17.